# Regulating supramolecular structure to enhance the ductility of regenerated cellulose films from ionic liquid solution

Yuanhao Li, Guangjie Song, Yoshiharu Nishiyama, Jun Zhang

# Regulating supramolecular structure to enhance the ductility of regenerated cellulose films from ionic liquid solution

*Yuanhao Li* [1,2], *Guangjie Song*[1,2]*, *Yoshiharu Nishiyama*[3], *Jun Zhang*[1,2]*

[1]Beijing National Laboratory for Molecular Sciences, CAS Key Laboratory of Engineering Plastics, Institute of Chemistry, Chinese Academy of Sciences, Beijing 100190, China

[2]University of Chinese Academy of Sciences, Beijing, 100039, China

[3]Univ. Grenoble Alpes, CNRS, CERMAV, 38000 Grenoble, France

* To whom all correspondence should be addressed.

Fax: +86-010-62613251

E-mail: gsong@iccas.ac.cn, jzhang@iccas.ac.cn

**Abstract**

Regenerated cellulose films suffer from inherent brittleness, restricting their practical use. Conventional plasticizer-based strategies can enhance ductility; however, plasticizer migration is an issue. Regulating supramolecular structure during processing is an alternative. We investigated the influence of coagulation bath temperature and coagulant types on the microstructure and mechanical properties of regenerated cellulose films using 1-allyl-3-methylimidazolium chloride (AmimCl) ionic liquid. The regeneration bath at 30°C yielded hydrogels with a fine, dense, uniform network compared to those at 60 ˚C or 90 ˚C. Simple drying of the uniform network resulted in films with increased elongation at break (~15%) while maintaining high tensile strength (~150 MPa). Solvent exchange to ethanol prior to drying preserved the hydrogel network, yielding dry films with elongation at break up to 30% and a tensile strength above 100 MPa. This property of film is related to the nanoscale structural heterogeneity: (1) a fine, dense and uniform network formed in the hydrogel; (2) lower density and hence looser packing due to the lower surface tension of ethanol. Thus, controlling coagulation conditions can effectively tailor nanoscale structural heterogeneity to significantly enhance ductility.

## 1. Introduction

Solution processing of cellulose has garnered increasing attention in recent years, particularly due to the emergence of environmentally friendly non-derivatizing solvents (Fink, Ganster, & Lehmann, 2014; Hermanutz, Vocht, Panzier, & Buchmeiser, 2019; Wang, Gurau, & Rogers, 2012; Wang, Lu, & Zhang, 2016; Zhang et al., 2017). Solvent systems such as NaOH/urea aqueous solutions (Cai et al., 2004), N-methylmorpholine-N-oxide (NMMO) (Fink, Weigel, & Bohn, 1999), and ionic liquids (ILs) (Asaadi et al., 2018) have been extensively investigated for cellulose dissolution. Among these, room-temperature ionic ILs have emerged as promising solvents due to their exceptional dissolution capacity, small vapor pressure, excellent thermal stability, and recyclability. Particularly, ILs including 1-allyl-3-methylimidazolium chloride (AmimCl) (Zhang, Wu, Zhang, & He, 2005) and 1-butyl-3-methylimidazolium chloride (BmimCl) (Swatloski, Spear, Holbrey, & Rogers, 2002) have demonstrated remarkable efficiency in dissolving unactivated pulp, yielding high-concentration cellulose solutions with minimal degradation. Fabrication of regenerated cellulose films with smooth surfaces and high transparency, while also avoiding the environmental burden and higher costs of traditional viscose production has been reported (Wan, Diao, Yu, Song, & Zhang, 2021; Zhang et al., 2017).

Despite these advantages, regenerated cellulose films suffer from inherent brittleness, which substantially restricts their practical applications. Neat cellulose films exhibit high modulus (~6 GPa) and tensile strength (~200 MPa) but low elongation at break (~12 %). Conventional approaches primarily utilize external plasticizers to enhance chain mobility, thereby improving material ductility (Sundberg, Toriz, & Gatenholm, 2013; Wei et al., 2025). Existing plasticizers such as glycerol in regenerated cellulose films can lead to larger ductility but with lower modulus and very often lower strength (Ahokas, Kunnari, Majoinen, Harlin, & Mäkelä, 2025). Thus, enhancing ductility of regenerated cellulose films while maintaining high tensile strength still remains a challenge. Also the addition of plasticizers has inherent problem of small molecule migration and exudation, leading to reduced stability of the material properties over time.

Regulation of supramolecular structure during processing provides an alternative pathway to enhance deformability without plasticizers. In particular, coagulation bath parameters including temperature, solvent type, and composition profoundly influence the microstructural evolution of cellulose gels, ultimately influencing the structure and properties of dried materials. The small angle neutron scattering studies showed coarser gel structure at a higher coagulation temperature from 1-ethyl-3-methylimidazolium acetate (EMIMAc) ionic liquid / DMSO mixture solution (Tiihonen, Bernardo, Dalgliesh, Mendes, & Parnell, 2024). By changing the coagulation temperature from 25 to 45 °C, tensile strength of the films prepared from NaOH/urea solution was varying in the range of 85–139 MPa (Li, Zhang, & Xu, 2012). However, how coagulation conditions govern the development of the cellulose gel microstructure and, consequently, the mechanical performance of dry films, is still unclear. We hypothesize that varying the type and temperature of the coagulation bath regulates gel structure during regeneration and the compaction during drying to create optimal nanoscale structure, which in turn enables enhancement of ductility.

Therefore, the present study examines the effects of coagulation bath type (water or ethanol) and temperature (30-90˚C) on the microstructure of cellulose films regenerated from AmimCl solutions. By correlating structural features with tensile properties of the dried films, we aim to elucidate how supramolecular structure can be leveraged to enhance the ductility.

## 2. Experimental Section

### 2.1. Chemicals

Dissolving grade wood pulp (alpha-cellulose content > 96%) was supplied by Bracell (Brazil) with a viscosity-average degree of polymerization (DPv) of 640, determined by Ubbelohde viscometer using copper(II) ethylenediamine solution (Sigma-Aldrich, analytical grade) as solvent. 1-Allyl-3-methylimidazolium chloride (AmimCl, purity > 99%) was synthesized and purified in our laboratory following previously established protocols (Zhang et al., 2005). Ethanol (99.7%, analytical grade) was purchased from Innochem.

### 2.2. Preparation of Cellulose/IL Solution

14 g wood pulp was first dried in a vacuum oven at 80°C and subsequently mixed with 186 g AmimCl at a 7:93 (w/w) ratio and kneaded in an IKA-Werk HKD-T06D mixer for 2 h under vacuum at 80°C to obtain a homogeneous 7 wt% solution. Dissolution was checked by polarized optical microscopy. We considered the absence of birefringent fiber fragments as a sign of complete dissolution.

### 2.3 Preparation of Cellulose Films

The 7 wt% cellulose/AmimCl solution was heated to 80°C. Approximately 1 g of the solution was then transferred onto a glass plate and spread into a uniform film with a thickness of 500 μm using a Baker-type 4-sided film applicator (Fig. 1a). For aqueous coagulation systems: The solution films were maintained at predetermined temperatures (90°C, 60°C, and 30°C) and subsequently immersed in water coagulation baths of the same temperature. This process yielded three distinct hydrogel films designated as gf-w90, gf-w60, and gf-w30, with the numbers corresponding to the coagulation temperatures. The gel film was then washed with water at least five times until $Cl^-$ ions in the washing solution could not be detected using 0.1 M $AgNO_3$ aqueous solution (Zhang et al., 2007).

For alternative coagulation systems: The cast films were first cooled to 30°C and then immersed in an ethanol coagulation bath maintained at 30°C for 30 minutes to produce ethanol-coagulated films (gf-e30). These films were subsequently washed with ethanol at room temperature.

Additionally, solvent exchange post-treatments were performed: we immersed the prepared gel films in approximately 200 mL of the exchange solvent, washed for 30 minutes, then replaced the exchange solvent and continued washing four more times to thoroughly remove the original solvent. (1) water-coagulated gf-w30 films were solvent-exchanged with ethanol to prepare gf-we30 samples, and (2) ethanol-coagulated gf-e30 films were exchanged with water to obtain gf-ew30 samples.

Film drying process: All gel films were mounted on glass plates and secured with adhesive tape along the edges. The samples were dried in an oven at 60°C for at least 1 hour. The central parts of the films were cut out for subsequent characterization and testing. Therefore, we obtained a total of six cellulose film gel samples, along with their corresponding dry film samples, as shown in Fig. 1b.

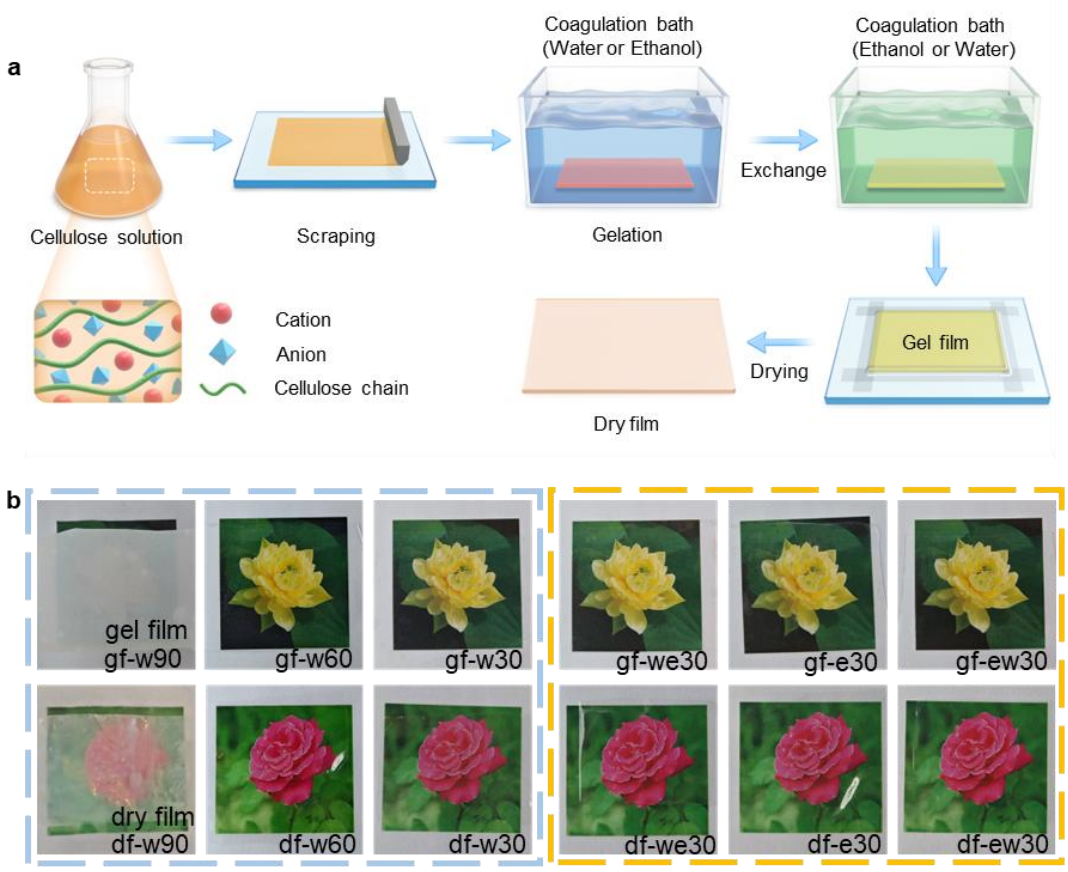


**Fig 1.** The preparation procedures (a) and the appearance(b) of regenerated cellulose films.

### 2.4 Characterization

We characterized the mechanical properties of regenerated cellulose dry films as well as the structures at different length scales, the morphology, density, and crystallinity of the dry films to understand the origin of difference in mechanical properties.

2.4.1 Mechanical Test

Dry film samples were cut into 50 mm (length) × 10 mm (width) strips along the scraper movement direction, equilibrated at 25°C and 50% relative humidity for 24 hours, and then subjected to mechanical testing. Tensile tests were performed using a universal testing machine (Instron 3365, INSTRON, USA) with a load capacity of 4000 N. All samples were tested under identical parameters: 20 mm gauge length, 2 mm/min crosshead speed. Film thickness was measured five times using a micrometer and averaged. Five valid measurements were obtained for each dry film sample.

2.4.2 Cryo-fracture surface of the films

Field-emission scanning electron microscope (Hitachi S-4800) was used to observe films cryo-fractured in liquid nitrogen and sputter-coated with approximately 5 nm platinum prior to observation. Imaging was conducted at 10 kV accelerating voltage.

2.4.3 Cryo-fracture surface of hydrogels

Hydrogel films mounted on specimen holders were high-pressure frozen using a Leica EM HPM100 system. The holders were transferred to the cryo-stage of a field-emission scanning microscope (Leica EM ACE600) via a vacuum cryo-transfer system (Leica EM VCT100).

Fracturing was performed under cryogenic conditions, followed by 15-minute sublimation at $2.8 \times 10^{-7}$ torr and 100 K to reveal surface morphology. The fracture surfaces were observed at -160°C using a secondary electron detector with an accelerating voltage of 2 kV.

2.4.4 X-ray Scattering

X-ray diffraction patterns were recorded in reflection mode (5-40° $2\theta$ range) using a PANalytical diffractometer (Netherlands) with Cu Kα radiation ($\lambda$ = 1.54 Å) at 2°/min scanning speed. Dry films were cut into small pieces and packed into standard sample holders.

Small-angle X-ray scattering (SAXS) measurements were performed at beamline BL16B of the Shanghai Synchrotron Radiation Facility (China). Both hydrogel and dry film samples were analyzed with 2 m specimen-to-detector distance (calibrated using AgBh powder) and 1.24 Å wavelength. Films were exposed with the incident perpendicular to the film surface for 120 s and the scattering was recorded using a Pilatus 2M detector (Dectris, Switzerland). The isotropic scattering was averaged over azimuthal angles. Background was subtracted after normalization with the transmission measured by a diode detector on the beamstop.

2.4.5 $^{13}$C CP/MAS Solid-State NMR Spectroscopy

Solid-state NMR spectra were acquired on a Bruker AVANCE III 600 spectrometer operating at 150 MHz for $^{13}$C with cross polarization and magic angle spinning (CP/MAS). Dry powder samples were packed in 4 mm zirconia rotors. Measurement parameters included: 8 kHz magic angle spinning, 2 s recycle delay, 10240 scans, and 1 ms contact time.

2.4.6 Transparency Measurement

Optical transmittance (200-800 nm) was measured using a UV-vis spectrophotometer (Shimadzu UV-2550). Films were directly mounted on sample holders and recorded at 1 nm intervals (32 scans total).

2.4.7 Density Measurement

We used floating method using mixed solutions of acetone and carbon tetrachloride. The liquid density at the suspending conditions was measured using a density tester (Brand: KEM, Model: DA-130N). Five measurements were taken for each sample, and the average value was calculated. The relative standard deviation was within 0.02%.

2.4.8 Thermogravimetric analysis (TGA):

Moisture content of the dry films was measured under a nitrogen atmosphere using a thermogravimetric analyzer (PerkinElmer TGA 8000). Prior to testing, the dry films were conditioned at 25 °C and 50% relative humidity (RH) for 12 h. The samples were heated from 30 to 130 °C at 10 °C/min and then held at 130 °C for 30 min to ensure complete removal of water.

The thermal stability of the dry films was evaluated in air using a thermogravimetric analyzer (PerkinElmer Pyris 1 TGA). The samples were heated from 50 to 600 °C at a rate of 10 °C/min.

## 3. Results and discussion

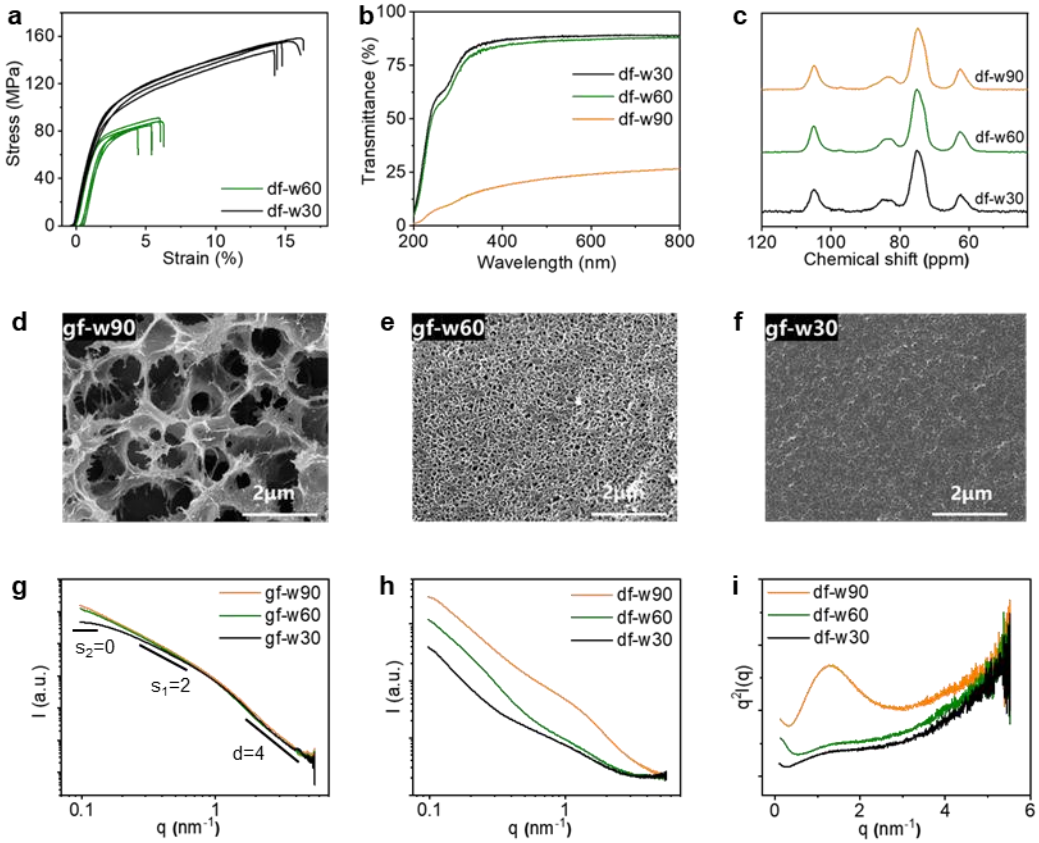


**Fig 2.** Structure and properties of regenerated cellulose films prepared at different coagulation bath temperatures. (a) Stress-strain curves of dry films (df-w30, df-w60, df-w90); (b) The transmittance of dry films (df-w30, df-w60, df-w90); (c) The $^{13}C$ CP/MAS solid-state NMR spectra of dry film powders (df-w30, df-w60, df-w90); (d-f) Cryo-SEM cross-sectional images of gel films (d) gf-w90, (e) gf-w60, and (f) gf-w30; (g-h) SAXS profiles of (g) gel films and (h) dry films; (i) Kratky plots of (h).

### 3.1 Effect of Coagulation Bath Temperature on the Structure and Properties of Dry Films

Among the three water regeneration bath temperatures, 30˚C (df-w30) exhibits the best mechanical performance, with a tensile strength of 160 MPa and an elongation at break of 15% (Fig 2a). The df-w60 had tensile strength and elongation at break dropping to 80 MPa and 6%, respectively. The df-w90 was too brittle to obtain valid stress-strain curves. These results indicate that coagulation at high temperatures significantly reduces both the tensile strength and ductility of regenerated cellulose films.

Both the gel films (gf-w30, gf-w60) and dry films (df-w30, df-w60) prepared at 30°C and 60°C were apparently uniform, characterized by smooth surfaces, and transparent features (Fig 1b). In contrast, samples prepared at 90°C (gf-w90 and df-w90) are white both before and after drying. UV-Vis spectra further confirm the optical clarity of df-w30 and df-w60 with a transmittance exceeding 87% in the visible light range (400~800 nm) (Fig. 2b). In comparison, the df-w90 only transmits about ~25% with little wavelength dependence. Furthermore gf-w90 even cracked during the drying process. All the three samples showed similar solid state 13C NMR spectra, with the absence of characteristic peak corresponding to C4 in crystals at 88-90 ppm (Fig.2c), indicating that all samples are essentially amorphous (Atalla, Gast, Sindorf, Bartuska, & Maciel,

1980).

All three gel samples exhibit open fibrous three-dimensional network structures under cryo-SEM, though the microfibril network dimension varies with coagulation bath temperature (Fig 2d-f) with higher temperature providing coarser structure. The gf-w90 sample displays pore sizes exceeding 1 μm that are unevenly distributed. In contrast, both gf-w60 and gf-w30 samples form more uniform nanoscale network structures, with average pore sizes of approximately 100 nm and 20 nm, respectively.

The SAXS data of gf-w90, gf-w60, and gf-w30 gel films (Fig. 2g) probes length scales from approximately 1.2 nm to 62 nm, corresponding to $2\pi/q_{max}$ for the smallest features ($q_{max}\approx5$ $nm^{-1}$) and $2\pi/q_{min}$ for the largest features ($q_{min}\approx0.1$ $nm^{-1}$). These plots all share a similar Porod exponent value of ~3.75 in the high-q region ($q > 0.7$ $nm^{-1}$), indicating comparable surface roughness of microfibrils regardless of the coagulation temperature. In the low-q region ($q < 0.7$ $nm^{-1}$), the "dimensionality" parameters s1 and s2 are used to characterize the shape of the corresponding scattering objects. In general, for scattering objects with spherical symmetry s1 = s2 = 0 and for cylindrical objects s1 = 1 and s2 = 0. For lamellae with equal width and length, the values are s1 = 2 and s2 =0 (Li, Senesi, & Lee, 2016). All three gel films show an $s_1$ value of ~2, suggesting that the fibrils are indeed ribbon like at least in the gel state. Significant differences are observed in the low q regions: gf-w30 exhibits a distinct $s_2 \approx 0$ feature, whereas gf-w60 and gf-w90 exhibits a consistent slope in $q < 0.2$ $nm^{-1}$, suggesting their higher heterogeneity in larger length-scale >30 nm with higher coagulation bath temperatures.

The SAXS data of dry films df-w90, df-w60, and df-w30 (Fig. 2h) show more pronounced difference than for the gel films, with the intensity decreasing over the whole q-range as the coagulation bath temperature decreases, indicating that the lower the coagulation temperature, the more homogeneous the final dry film. The scattering intensity shows a clear correlation with the density differences among the dry films: df-w30 (1.520 $g/cm^3$)>df-w60 (1.512 $g/cm^3$)> df-w90 (1.503 $g/cm^3$) (Fig. S1). In the Kratky plot (Fig. 2i) of df-w30 and df-w60 display a broad, low-intensity peak at $q = 1.2$ $nm^{-1}$, whereas df-w90 exhibits a pronounced peak at the same position, reflecting electron density fluctuation at 5 nm length scale.

Based on these results, 30°C is selected as the optimal coagulation bath temperature for subsequent studies.

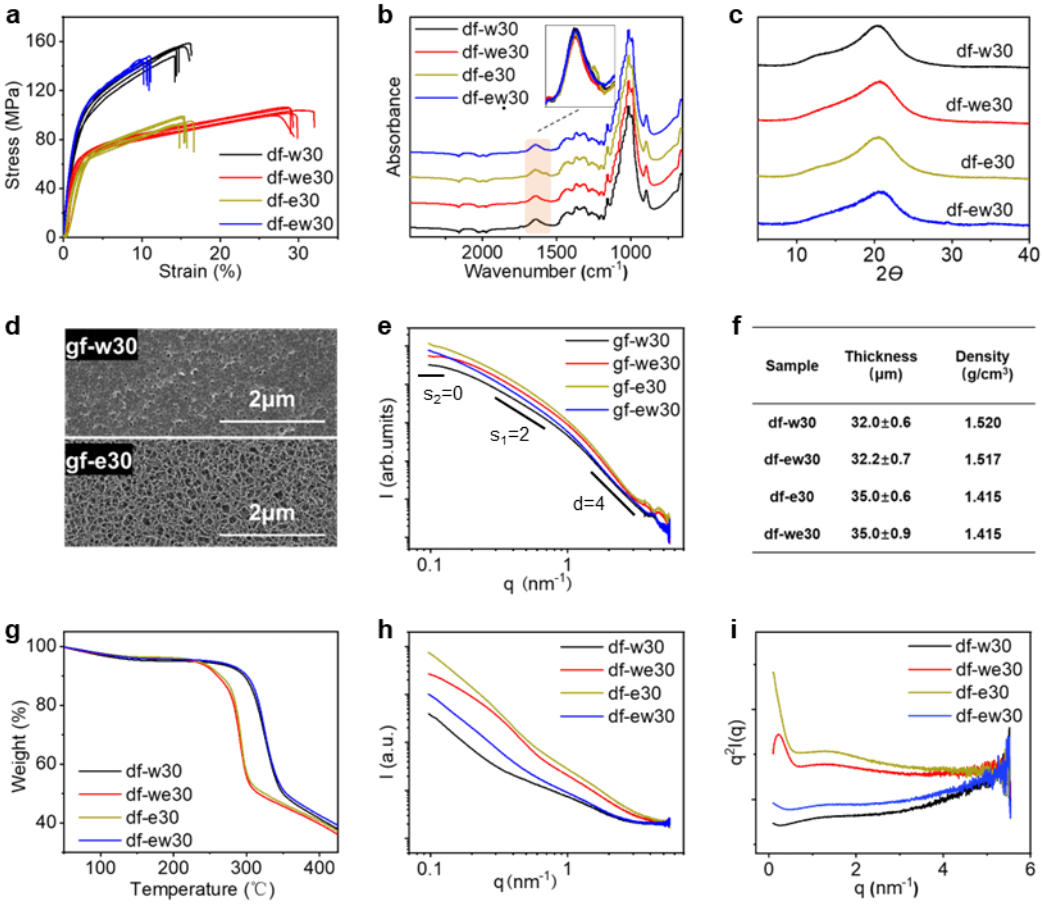


**Fig 3.** Structure and properties of regenerated cellulose films prepared from different coagulation baths. (a) Stress-strain curves of dry films (df-w30, df-we30, df-e30, df-ew30); (b) FTIR spectra of dry films with the light orange rectangle highlighting the δ(OH) bending vibration at 1648 $cm^{-1}$; (c) XRD patterns of dry films; (d) Cryo-SEM cross-sectional images of gel films gf-w30 and gf-e30; (e) SAXS profiles of gel films (gf-w30, gf-we30, gf-e30, gf-ew30); (f) Thickness and suspended density of dry films (df-w30, df-we30, df-e30, df-ew30); (g) TGA thermograms of dry films; (h) SAXS profiles of dry films (df-w30, df-we30, df-e30, df-ew30); (i) Kratky plots corresponding to (h).

### 3.2 Effect of Coagulation Bath Types on the Structure and Properties of Dry Films

To separate the effect of coagulation bath media and drying-induced structural changes, we prepared three sample sets based on the gf-w30/df-w30 system: (1) hydrogel-ethanol exchange (gf-we30/df-we30), (2) pure ethanol coagulation bath (gf-e30/df-e30), and (3) ethanol gel-water solvent exchange (gf-ew30/df-ew30). All gel films (gf-w30, gf-we30, gf-e30, and gf-ew30) were similar in macroscopic appearance, and the corresponding dry films (df-w30, df-we30, df-e30, and df-ew30) remained colorless and transparent (Fig 1b, Fig. S2 and S3).

The tensile properties of regenerated cellulose films varied significantly depending on the coagulation bath treatment (Fig. 3a). The water-coagulated and ethanol-exchanged df-we30 sample shows the highest ductility, with an elongation at break of 30%—twice that of the water-coagulated df-w30 (15%)—though its tensile strength decreases from 150 MPa to 100 MPa. Notably, the ethanol-coagulated df-e30 and dried-from-ethanol sample exhibits the lowest

mechanical strength (95 MPa) and an elongation at break of 15%. In contrast, when the ethanol gel was solvent exchanged to water prior to drying, the resulting df-ew30 sample showed a significantly enhanced tensile strength (140 MPa) but a reduced elongation at break (11%). The yield stress seems to be governed by the media from which the sample was dried: 70 MPa for ethanol and 100 MPa for water, while the elongation at break is governed by the coagulation bath: larger for water than ethanol.

Both XRD and NMR spectra shows similar profiles for df-w30, df-ew30, df-e30, and df-we30, corresponding to amorphous cellulose by the absence of crystalline diffraction peaks (Fig. 3c) and the absence of 88-90 ppm regarding to the crystalline C4 peak (Fig. S4) (Atalla et al., 1980). This rules out crystallinity as a contributing factor to the mechanical property variations.

To check the water content of the films, we performed FTIR and TGA. Previous studies have demonstrated that water acts as a plasticizer in the amorphous regions of cellulose, significantly affecting mechanical properties (Sundberg et al., 2013). FTIR spectra (Fig. 3b) show nearly identical peak intensities at 1640 $cm^{-1}$ which is characteristic water absorption band (Bayly, Kartha, & Stevens, 1963), indicating similar water contents across all samples. The weight loss at 180˚C under nitrogen flow (Fig. S5) showed was around 9.7% within 0.4% for all samples of df-w30 (9.8%), df-we30 (9.9%), df-e30 (9.3%), and df-ew30 (10.1%). Thus, the effect of water content in the difference in mechanical performance would be negligible.

### 3.3 Mechanism of Enhanced Ductility in Cellulose Films

Regenerated cellulose gel films prepared in aqueous (gf-w30) and ethanol-based (gf-ew30) coagulation baths, exhibited distinct network morphologies (Fig 3d): the ethanol-coagulated gf-ew30 sample has significantly larger pore sizes than the water-coagulated gf-w30 sample. The aqueous coagulation promotes the formation of a finer gel network.

The SAXS in the high-q region ($q > 0.7\ nm^{-1}$) in same solvent medium (e.g., gf-w30 vs. gf-ew30, gf-we30 vs. gf-e30) exhibit nearly identical scattering curves, while in the low-q region ($q < 0.1\ nm^{-1}$), gel samples formed in the same coagulation bath (e.g., gf-w30 vs. gf-we30, gf-e30 vs. gf-ew30) display similar intensity. This phenomenon clearly demonstrates that the coagulation bath plays a decisive role in shaping the gel network structure at higher length scale, whereas the local structure can be altered by solvent exchange.

In the high-q region ($q > 0.7\ nm^{-1}$), Porod exponent value of aqueous gel samples gf-w30 and gf-ew30 (3.75) is lower than that of ethanol gel samples gf-we30 and gf-e30 ($d \approx 4$), indicating that the microfibril networks formed in aqueous coagulation baths exhibit rougher surfaces or more graduate transition between network and pore. In the low-q region ($q < 0.7\ nm^{-1}$), all samples show an $s_1$ value of approximately 2, suggesting that cellulose form ribbon like structure in the gel state. However, aqueous-coagulated samples (gf-w30 and gf-we30) exhibit an $s_2$ value of zero, while ethanol-coagulated samples (gf-e30 and gf-ew30) display no distinct $s_1$ -$s_2$ transition, suggesting more heterogeneity in the $q < 0.2\ nm^{-1}$ regime in the latter.

Comparative analysis of thickness variations among different dry film samples (Fig. 3f) reveals that df-w30 and df-ew30 samples are consistently thinner by approximately 3 μm (8.6% reduction) compared to df-e30 and df-we30 samples, corroborating the higher density (~1.520 $g/cm^3$) of the dry films derived from aqueous gel systems (df-w30 and df-ew30), compared to the ~1.415 $g/cm^3$ of the film from the ethanol gel systems (df-e30 and df-we30) corresponding to 6.9% difference. These findings align with the previous research that aqueous gels undergo significant

contraction during drying, forming densely packed aggregates, whereas ethanol gels maintain relatively loose structure (Li et al., 2020). This distinction primarily stems from stronger capillary forces in aqueous systems during drying, promoting tighter molecular packing.

To further validate these conclusions, we conducted TGA analysis of the four dry film samples. Thermal degradation experiments (Fig. 3g) clearly show that ethanol-derived samples (df-e30 and df-we30) begin weight loss at 220°C, which is 50°C lower than their aqueous-derived counterparts (df-w30 and df-ew30 at 270°C). Notably, dry films from gels with identical solvent media exhibit nearly overlapping pyrolysis curves. These thermal analysis results provide additional evidence that ethanol coagulation leads to looser packing in dry films, resulting in significantly reduced temperatures for the weight-loss event. Often the weight loss is interpreted as thermal decomposition, but in this case, the decomposition starts probably at 220 ˚C in both case. The volatile compound such as levoglucosan cannot evaporate in a tightly closed structure leading to the weight loss at higher temperature. The fact that a freeze-dried film also shows lower temperature of weight-loss in Fig. S6 confirmed that the lower weight-loss temperature originates from the porosity.

SAXS (Fig. 3h) intensities, normalized for film thicknesses, show differences among the four dry film samples: the aqueous gel-dried df-w30 sample exhibits the lowest scattering intensity, while the ethanol gel-dried df-e30 sample shows the highest intensity, with solvent-exchanged df-we30 and df-ew30 samples displaying intermediate values. These findings are fully consistent with our previous conclusion that aqueous gel drying produces more homogeneous structures.

When plotted in Kratky style (Fig. 3i), aqueous gel-dried samples (df-w30 and df-ew30) show a broad, low-intensity peak at $q = 1.2\ nm^{-1}$. In contrast, ethanol gel-dried samples of df-we30 show a sharp peak at $q = 0.22\ nm^{-1}$ (corresponding to a 28 nm scale) suggesting the presence of structural heterogeneity, while much higher intensity of df-e30 toward the low-q region implies larger-scale (>30 nm) heterogeneity. These nanoscale structural differences—particularly the pronounced structural heterogeneity in the ethanol gel-dried df-e30 sample—likely serve as a key factor in its reduced mechanical performance since the strength of the material is governed by the presence of weak points. Therefore, the significantly enhanced ductility of df-we30 can be primarily attributed to its unique structural characteristics: relatively loose molecular packing with nanoscale heterogeneity that allows large deformation but homogeneous at a larger length scale avoiding stress concentration.

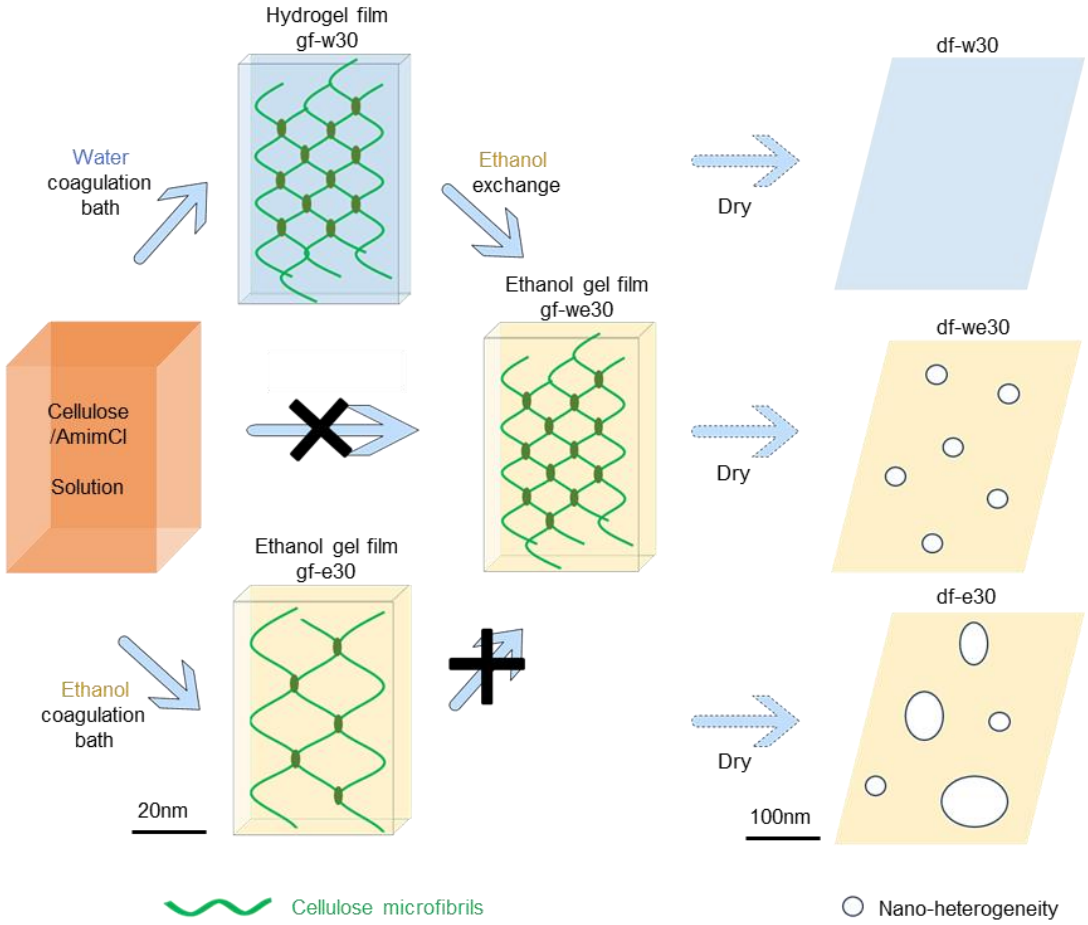


**Fig 4.** Schematic illustration of the ductility enhancement mechanism in regenerated cellulose films.

Based on the above analyses, achieving highly ductile regenerated cellulose films requires two key conditions: (1) a fine, dense and uniform network in gel state, and (2) loosely chain packing that can be induced by ethanol drying. The homogeneous hydrogel network is first formed by low-temperature water bath, and then solvent exchanged to low-surface tension solvent before drying (Fig. 4). This approach enabled the production of regenerated cellulose films with doubled elongation at break (up to 30%) while maintaining the tensile strength (~100 MPa).

## 4. Conclusions

The coagulation bath temperature has significant impact on the homogeneity and the tensile strength of regenerated cellulose films, with lower temperature leading to stronger film with larger elongation at break. At a low coagulation temperature of 30°C the dry film showed 150 MPa tensile strength and 15% elongation at break. Combining this low-temperature coagulation with ethanol solvent exchange preserves the hydrogel network, enabling the strength–ductility balance of dry films with elongation at break reaching 30%, but still keeping the tensile strength of 100 MPa. The low-temperature coagulation process produces gels with a fine, dense and uniform network, which can explain the superior mechanical property of dry films. Network structure of hydrogel films can be retained in ethanol gels through solvent exchange, followed by drying to

prepare highly ductile films. This improvement is probably due to (1) a fine, dense and uniform network formed in the hydrogel state; (2) looser chain packing induced by ethanol drying, creating optimal nanoscale structural heterogeneity. The synergistic application of our supramolecular structure regulation approach and traditional glycerol plasticization will further enhance the film's ductility. This work provides a novel approach for designing highly ductile cellulose materials.

**Acknowledgement**

We thank the Shanghai Synchrotron Radiation Facility of BL16B1(https://cstr.cn/31124.02.SSRF.BL16B1) for the assistance on SAXS measurements, International Partnership Program of the Chinese Academy of Sciences No. 027GJHZ2024087GC.

**References:**

Ahokas, P., Kunnari, V., Majoinen, J., Harlin, A., & Mäkelä, M. (2025). Plasticizer Mixing Improved Regenerated Cellulose Films as an Alternative to Plastics. *ACS Sustainable Chemistry & Engineering,* 13(28), 10771-10779.

Asaadi, S., Hummel, M., Ahvenainen, P., Gubitosi, M., Olsson, U., & Sixta, H. (2018). Structural analysis of Ioncell-F fibres from birch wood. *Carbohydrate Polymers,* 181, 893-901.

Atalla, R. H., Gast, J. C., Sindorf, D. W., Bartuska, V. J., & Maciel, G. E. (1980). Carbon-13 NMR spectra of cellulose polymorphs. *Journal of the American Chemical Society,* 102(9), 3249-3251.

Bayly, J. G., Kartha, V. B., & Stevens, W. H. (1963). The absorption spectra of liquid phase H2O, HDO and D2O from 0·7 μm to 10 μm. *Infrared Physics,* 3(4), 211-222.

Cai, J., Zhang, L. N., Zhou, J. P., Li, H., Chen, H., & Jin, H. M. (2004). Novel fibers prepared from cellulose in NaOH/urea aqueous solution. *Macromolecular Rapid Communications,* 25(17), 1558-1562.

Fink, H.-P., Ganster, J., & Lehmann, A. (2014). Progress in cellulose shaping: 20 years industrial case studies at Fraunhofer IAP. *Cellulose,* 21(1), 31-51.

383 Fink, H.-P., Weigel, P., & Bohn, A. (1999). Supermolecular structure and orientation of blown
384 cellulosic films. *Journal of Macromolecular Science, Part B,* 38(5-6), 603-613.
385 Hermanutz, F., Vocht, M. P., Panzier, N., & Buchmeiser, M. R. (2019). Processing of
386 Cellulose Using Ionic Liquids. *Macromolecular Materials and Engineering,* 304(2),
387 1800450.
388 Li, H., Kruteva, M., Mystek, K., Dulle, M., Ji, W., Pettersson, T., & Wågberg, L. (2020). Macro-
389 and Microstructural Evolution during Drying of Regenerated Cellulose Beads. *ACS*
390 *Nano,* 14(6), 6774-6784.
391 Li, R., Zhang, L., & Xu, M. (2012). Novel regenerated cellulose films prepared by coagulating
392 with water: Structure and properties. *Carbohydrate Polymers,* 87(1), 95-100.
393 Li, T., Senesi, A. J., & Lee, B. (2016). Small Angle X-ray Scattering for Nanoparticle Research.
394 *Chemical Reviews,* 116(18), 11128-11180.
395 Sundberg, J., Toriz, G., & Gatenholm, P. (2013). Moisture induced plasticity of amorphous
396 cellulose films from ionic liquid. *Polymer,* 54(24), 6555-6560.
397 Swatloski, R. P., Spear, S. K., Holbrey, J. D., & Rogers, R. D. (2002). Dissolution of cellulose
398 with ionic liquids. *Journal of the American Chemical Society,* 124(18), 4974-4975.
399 Tiihonen, L. V., Bernardo, G., Dalgliesh, R., Mendes, A., & Parnell, S. R. (2024). Influence of
400 the coagulation bath on the nanostructure of cellulose films regenerated from an ionic
401 liquid solution. *Rsc Advances,* 14(18), 12888-12896.
402 Wan, J., Diao, H., Yu, J., Song, G., & Zhang, J. (2021). A biaxially stretched cellulose film
403 prepared from ionic liquid solution. *Carbohydrate Polymers,* 260.
404 Wang, H., Gurau, G., & Rogers, R. D. (2012). Ionic liquid processing of cellulose. *Chemical*

*Society Reviews,* 41(4), 1519-1537.

Wang, S., Lu, A., & Zhang, L. (2016). Recent advances in regenerated cellulose materials. *Progress in Polymer Science,* 53, 169-206.

Wei, P., Zhang, Z., Cheng, S., Meng, Y., Tong, M., Emu, L., . . . Jiang, H. (2025). Biodegradable origami enables closed-loop sustainable robotic systems. 11(6), eads0217.

Zhang, H., Wang, Z., Zhang, Z., Wu, J., Zhang, J., & He, H. (2007). Regenerated-cellulose/multiwalled-carbon-nanotube composite fibers with enhanced mechanical properties prepared with the ionic liquid 1-allyl-3-methylimidazolium chloride. *Advanced Materials,* 19(5), 698-704.

Zhang, H., Wu, J., Zhang, J., & He, J. (2005). 1-Allyl-3-methylimidazolium Chloride Room Temperature Ionic Liquid: A New and Powerful Nonderivatizing Solvent for Cellulose. *Macromolecules,* 38(20), 8272-8277.

Zhang, J., Wu, J., Yu, J., Zhang, X., He, J., & Zhang, J. (2017). Application of ionic liquids for dissolving cellulose and fabricating cellulose-based materials: state of the art and future trends. *Materials Chemistry Frontiers,* 1(7), 1273-1290.